SPECIAL
NASA HS3
COLLECTION

# Observations and Predictability of a Nondeveloping Tropical Disturbance over the Eastern Atlantic

ALAN BRAMMER AND CHRIS D. THORNCROFT

*Department of Atmospheric and Environmental Science, University at Albany, State University of New York, Albany, New York*

JASON P. DUNION

*NOAA/Atlantic Oceanographic and Meteorological Laboratory/Hurricane Research Division, and Rosenstiel School of Marine and Atmospheric Science, University of Miami, Miami, Florida*

(Manuscript received 21 February 2018, in final form 9 July 2018)

ABSTRACT

A strong African easterly wave (AEW) left the West African coast in early September 2014 and operational global numerical forecasts suggested a potential for rapid tropical cyclogenesis of this disturbance in the eastern Atlantic, despite the presence of a large region of dry air northwest of the disturbance. Analysis and in situ observations show that after leaving the coast, the closed circulation associated with the AEW trough was not well aligned vertically, and therefore, low-level or midlevel dry air was advected below or above, respectively, areas of closed circulation. GPS dropwindsonde observations highlight the dry air undercutting the midlevel recirculation region in the southwestern quadrant. This advection of dry air constrains the spatial extent of deep convection within the AEW trough, leading to the vortex decaying. As the column continues to be displaced horizontally, losing vertical alignment, this enables increased horizontal advection of dry air into the system further limiting convective activity. Ensemble forecasts indicate that short-term errors in precipitation rate and vorticity generation can lead to an over intensified and well-aligned vortex, which then interacts less with the unfavorable environment, allowing for further convection and intensification. The stronger vortex provides more favorable conditions for precipitation through a more vertically coherent closed circulation and thus a positive feedback loop is initiated. The short-term forecasts of precipitation were shown to be sensitive to lower-tropospheric moisture anomalies around the AEW trough through ensemble sensitivity analysis from Global Ensemble Forecast System real-time forecasts.

## 1. Introduction

Tropical cyclogenesis is known to be favored by several large-scale conditions, including a preexisting low-level disturbance, warm SSTs (≥26.5°C), increased low- and midlevel moisture around the disturbance, and relatively low environmental vertical wind shear (Gray 1968). These conditions typically favor the maintenance of deep convection associated with the tropical cyclogenesis process. Over the eastern Atlantic, African easterly waves (AEWs) propagate from West Africa with cyclonic vorticity maximized near the level of the African easterly jet (AEJ) around 700–600 hPa (e.g., Burpee 1972, 1974). These AEW troughs provide the preexisting low-level vortex for around 50% of tropical cyclogenesis events over the tropical Atlantic (e.g., Carlson 1969a,b; Frank 1970; Landsea 1993). As the AEW troughs transit over the coastal region of West Africa, deep convection and associated potential vorticity generation can be a crucial stage in the AEW life cycle for developing low-level vorticity (e.g., Berry and Thorncroft 2005). Multiple factors (e.g., MJO, convectively coupled Kelvin waves, the local diurnal cycle, and midlatitude troughs) have been shown to influence deep convection around the West African coastal region and have been linked to influencing tropical cyclone (TC) genesis from AEW troughs over the eastern Atlantic (e.g., Bracken and Bosart 2000; Chiao and Jenkins 2010; Ventrice et al. 2012).

Composite analyses of developing and nondeveloping AEWs have revealed synoptic-scale differences that help explain why only around 15% of AEWs lead to

*Corresponding author*: Alan Brammer, abrammer@albany.edu

DOI: 10.1175/MWR-D-18-0065.1

tropical cyclogenesis events. Hopsch et al. (2010) showed that developing AEW troughs already had stronger low-level vorticity and increased ascent over the coastal region prior to leaving the African continent. The ability for deep convection to be sustained as the AEWs leave the coast is important for maintaining and continuing the intensification of the vortex (Arnault and Roux 2009, 2010), though at this point in the pregenesis cycle, the areal coverage of deep convection can be more important than the intensity of the convection (Leppert et al. 2013a,b).

The modulation of synoptic-scale thermodynamics by AEWs is especially important for convective activity over the eastern Atlantic given the typical presence of dry air north of the AEJ, either of Saharan origin [i.e., the Saharan air layer (SAL)] or subsidence from the subtropics or midlatitudes (Dunion and Velden 2004; Braun 2010; Brammer and Thorncroft 2015). In a Lagrangian reference frame a strong horizontal circulation around the AEW trough can potentially provide a protected region of closed circulation with favorable thermodynamics that supports continued convection and intensification (Dunkerton et al. 2009). However, AEWs over West Africa are typically cold core at low levels, developing low-level vorticity as they leave the coast and transition into the oceanic environment off the West Africa coast (Janiga and Thorncroft 2013). Therefore, regions with closed circulations at the level of the AEJ will likely not have a closed circulation above or below the vortex at this stage of the life cycle (Wang and Hankes 2014). Convective activity within the AEW trough can therefore be influenced by the surrounding environment. Intensifying MCSs around the West African coastal region typically experience increased low-level southerly moisture flux associated with the downstream AEW trough (Dieng et al. 2014). Similarly, differences in low-level moisture downstream (i.e., west northwest) of strong AEW troughs was shown to be a significant differentiating factor in the composite analysis of developing and nondeveloping AEWs (Brammer and Thorncroft 2015). Fritz and Wang (2013) showed that midlevel dry air intrusions were also associated with suppressed convection and a halting in the intensification of an otherwise favorable AEW trough over the Atlantic main development region. While Freismuth et al. (2016) showed how the influx of dry air into a weakened disturbance can hinder convection leading to a reduction in vorticity and further entrainment of dry air.

Ensemble numerical simulations of tropical cyclogenesis cases have also highlighted the impact of the variability in the moisture field around pregenesis tropical disturbances. Variability in the initial conditions of moisture and convective available potential energy (CAPE) within the AEW trough or incipient vortex can affect the short-term spinup of the vortex, creating large ensemble spread in vortex strength that continues to amplify through the forecast (Torn and Cook 2013). Ensemble-based sensitivity analyses for forecasts of AEWs over West Africa, as well as tropical cyclogenesis events that are linked to AEWs, have shown significant correlation between moisture west and north of the AEW trough in the initial conditions and the forecast intensity of the disturbance (Torn 2010; Rios-Berrios et al. 2016). The sensitivity to the initial AEW trough characteristics and synoptic-scale environmental characteristics highlight the potential difficulties for operational numerical forecasts of tropical cyclogenesis. Komaromi and Majumdar (2015) showed that forecasts of tropical cyclogenesis were sensitive to both the predictability of the forecasted environment as well as the strength and location of the pregenesis disturbances. The eastern Atlantic has also been shown to be a region of high false alarm rates for deterministic tropical cyclogenesis forecasts from global models (Halperin et al. 2013) suggesting a need for further study to understand model biases and processes that influence TC genesis in this region of the Atlantic basin.

In 2014, the NASA Hurricane and Severe Storm Sentinel (HS3) field campaign observed Atlantic tropical systems with a high-altitude Global Hawk unmanned aircraft system (UAS; Braun et al. 2016). Because of its long duration (~24 h), extended range (~15 000–18 500 km), and high operating altitude (~16.7–19.8 km), the Global Hawk was able to collect in situ observations from the lower stratosphere to the ocean surface in tropical systems as far east as around 30°W. Given the uncertainty regarding the influence of the SAL or other sources of dry air (e.g., midlatitude dry air intrusions; Dunion 2011) on developing disturbances, this platform provided a unique opportunity to observe potential cyclogenesis events over the eastern Atlantic. This paper documents the evolution and forecasts of a nondeveloping disturbance that was designated by the NOAA National Hurricane Center (NHC) as Invest AL90 during the first week of September 2014. While previous research has compared ensemble forecasts for developing cases or provided analysis for developing and nondeveloping cases, there are no detailed analyses of the forecasts or predictability of strong nondeveloping AEW troughs.

A synoptic overview of the AEW trough associated with AL90 will be presented in section 3. This section will include analyses of the observations and reanalysis structure of the AEW trough. Section 4 will then include analyses of the Global Ensemble Forecast System (GEFS) operational ensemble forecasts of the disturbance and forecasts for tropical cyclogenesis over the eastern Atlantic. A discussion of the observed evolution

of AL90 in contrast to numerical simulations of the tropical disturbance will follow in section 5.

## 2. Data and methodology

Climate Forecast System (CFS), version 2, data were used for the analysis of the evolution of the AEW trough and for verification against the model ensemble forecasts, with climatological values calculated with respect to the CFS Reanalysis (CFSR) for the period of 1979–2010 (Saha et al. 2010, 2014). MERRA2 is also utilized to represent dust around the AEW trough.

Observations from the HS3 Global Hawk platform include GPS dropwindsondes (dropsondes) that provide vertical profiles of temperature, relative humidity, and winds (Hock and Franklin 1999), as well as the NASA Cloud Physics Lidar (CPL), which is able to detect multiple layers of aerosol throughout the troposphere. Dropsondes were postprocessed through the automatic sounding quality control software, the Atmospheric Sounding Processing Environment (ASPEN; Wang et al. 2010) and reprocessed to correct for an upper-level dry bias (Vomel et al. 2016). Observed precipitation rates are obtained from the NASA Tropical Rainfall Measuring Mission (TRMM) Multisatellite Precipitation Analysis (TMPA; TRMM product 3B42; Huffman et al. 2007). Ensemble forecasts are analyzed from the 21-member operational NCEP GEFS archived at NOAA's National Centers for Environmental Information (NCEI) website.

The AEW trough associated with AL90 is tracked objectively utilizing a multiple variable tracker similar to the NCEP TC tracker (Marchok 2002). Tracking is carried out by analyzing mass-weighted centers across multiple levels and multiple fields (curvature vorticity at 850, 700, and 500 hPa; geopotential height at 850 hPa; and relative vorticity at 850 and 700 hPa). A single center is then found through averaging the multiple potential centers that fall within a 300-km tolerance of the estimated center. Tracking both relative and curvature vorticity at multiple levels enables a smooth and continuous track across the circulation associated with the AEW trough or more well-defined tropical disturbances. Propagation of the disturbance is calculated as a combination of extrapolation of the previous phase speed and axisymmetric steering flow calculated over the 850–400-hPa layer and out to a radius of 400 km from the disturbance center. Ensemble forecast tracks follow the same tracking criteria using the analysis position as the initial estimated location for each 0000 UTC initialization time. Analysis locations are then recentered in each ensemble to account for the perturbations in the initial conditions.

## 3. AEW synoptic history

### a. Synoptic evolution

Invest AL90 in September 2014 was associated with the trough of a well-defined AEW. The trough can be traced back to Ethiopia on 27 August (not shown), with active convection across the Sahel region (Fig. 1a). As the AEW trough left the West African coast on 4 September, the NHC declared the system as Invest AL90. The NHC 5-day genesis forecast probabilities for AL90 peaked at 40% at 1800 UTC 4 September. Given the evolution of the AEW trough across the African continent, with local SSTs over 28°C, deep-layer (200–850 hPa) vertical wind shear below 5 m $s^{-1}$, and the bullish global model forecasts at the time, this invest was of particular interest to the NASA HS3 field campaign. The Global Hawk was flown from 1800 UTC 5 September to 0400 UTC 6 September and collected a variety of in situ and remote sensing data in AL90 and its surrounding environment.

The accumulated precipitation field in Fig. 1a shows that the AEW trough had regular convection around the circulation center as it moved across the Sahel. A vortex-centric time series of infrared (IR) brightness temperature coverage, precipitation rate, 850–600-hPa layer-averaged circulation (relative vorticity averaged over a radius of 300 km), and the surrounding (300–750-km annulus) 850-hPa specific humidity also highlights this evolution (Fig. 2). The time series shows that the AEW trough was associated with a significant diurnal cycle in precipitation while over the land, exhibiting consistent evening peaks for the period from 28 August to 3 September with only one exception on the evening of 31 August. Low-level circulation and environmental humidity during this continental stage of the AEW life cycle remained relatively constant until the trough approached the coast (3 September). After reaching the coast around 4 September, the low-level circulation increased slightly for a few hours but then decreased rapidly, consistent with a lack of development. During this oceanic stage, both the precipitation associated with the system and environmental humidity are reduced compared to the continental stage.

Figure 3 displays the vertical structure of the vorticity, the horizontal winds, and the 6-h change in specific humidity averaged over a radius of 300 km around the AEW trough center. During the AEW trough's continental transit (28 August–3 September), the AEW trough shows the typical 700–600-hPa jet-level maximum in vorticity with weak horizontal winds averaged over a radius of 300 km, suggesting the presence of a nearly symmetric wave relative circulation. However, at

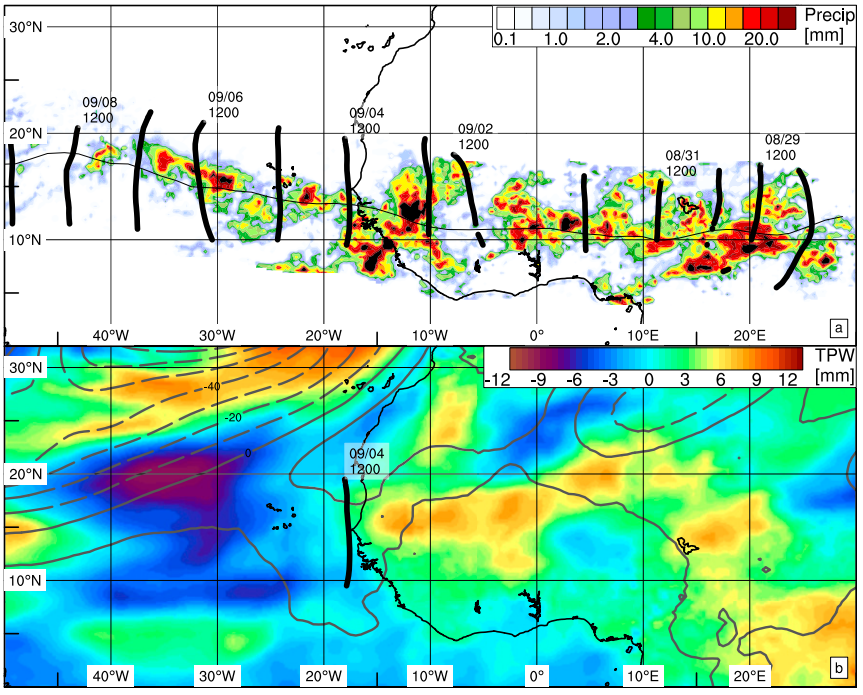


FIG. 1. (a) Accumulated precipitation following pre-AL90 vortex (within 750 km), vertical black lines show objective trough axes every 24 h. Thin black line shows vortex track. (b) Daily mean anomalous total precipitable water (shading) and anomalous 300-hPa geopotential height (contours) and objective AEW trough line for 1200 UTC 4 Sep.

low levels there was strong wave-relative westerly flow associated with the background monsoon flow and the phase speed of the AEW trough. Specific humidity changes around the AEW trough exhibit small diurnal fluctuations but does not indicate any long-term moistening or drying at any level. This continental evolution of the AEW is representative of a well-defined and convectively active AEW trough similar to the evolution of the intense AEW documented in Berry and Thorncroft (2005).

As the AEW trough reaches the coast, the 300–750-km annulus-averaged environmental specific humidity at 850 hPa drops abruptly from 12–13 to 10 g kg$^{-1}$ (see Fig. 2), consistent with the change in the large-scale environment shown by the anomalous total precipitable water field in Fig. 1b. Moisture within 300 km of the AEW trough axis also exhibited a small negative trend during the evening of 3 September between ~400 hPa and the surface (Fig. 3). As the AEW trough transited the coastal region, the vorticity started to increase at low levels (925–850 hPa) although it subsequently weakened at the jet level. This low-level increase in vorticity is consistent with the climatological evolution of AEWs and enhanced precipitation over the coastal region shown by Janiga and Thorncroft (2013). However, in the days after leaving the coast, only scattered precipitation was present with a relatively weak area-averaged intensity (Fig. 2). The NASA HS3 Global Hawk flight sampled the system a day after leaving the West African coast during the evening of 5 September (represented by the shaded background in Fig. 2) as the vorticity throughout the trough was weakening.

Figure 4 presents the wave-relative circulation at 500 and 850 hPa together with equivalent potential temperature $\theta_e$ and precipitation at three times after the trough had left the West African coast. Corresponding vertical cross sections are shown in Fig. 5 latitudinally averaged over ±2° from the vortex center. At 1800 UTC 4 September, the AEW trough at 500 hPa was characterized by a well-defined, though meridionally elongated, closed circulation located around (13°N, 21°W) within a much broader cyclonic region between about 25° and 15°W (Fig. 4a). At 850 hPa there was a similarly broad large-scale trough but with a much smaller closed circulation located east of the closed circulation at 500 hPa (Fig. 4d). Precipitation associated with the trough was collocated with the center of closed circulation at 500 hPa but was on the western edge of the closed circulation at 850 hPa. At both levels $\theta_e$ exceeded 336 K within the region of closed circulation, though low $\theta_e$ (≤330 K) can be seen wrapping around the outside of the circulation on the western and southern flanks.

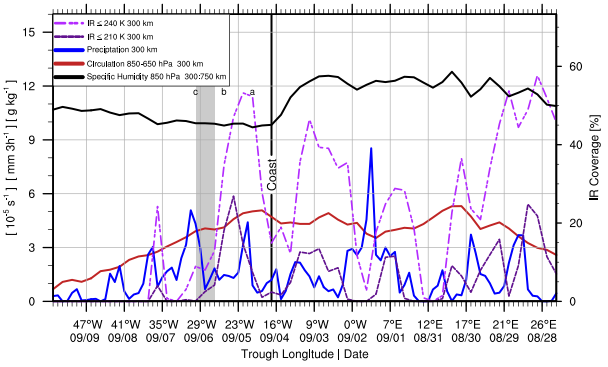


FIG. 2. Trough-centric time series of analysis and observational variables. GridSat IR areal coverage (dashed purple) and TRMM mean precipitation rate (solid blue) are extracted over a 300-km radius around the vortex maximum. CFSv2 specific humidity (850 hPa) is averaged over an annulus of 300–750 km from the vortex center (solid black line). CFSv2 850–600-hPa circulation calculated over a radius of 300 km (solid red line). Vertical line denotes coastal passage, gray shading represents the NASA HS3 Global Hawk sampling period. Corresponding times from Fig. 4 are denoted by the lowercase letters.

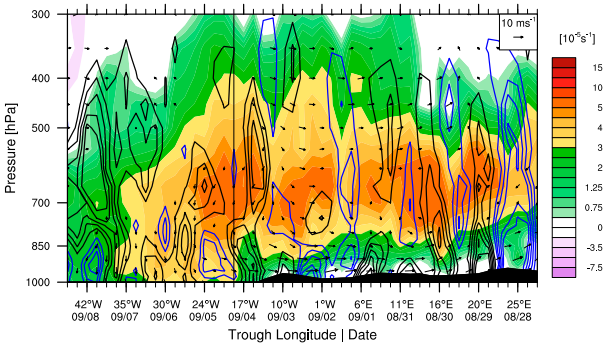


FIG. 3. Vertical profile evolution for 6-hourly variables averaged over 300 km around the trough center. Relative vorticity (background shading), the 6-hourly change in specific humidity [blue (black) contours for positive (negative) 0.5 g kg$^{-1}$ day$^{-1}$], and wave-relative zonal and meridional wind (vectors; the top of the plot represents north for meridional wind). Surface intersecting isobars are masked. Vertical line at 0600 UTC 4 Sep represents troughs transit over the coast.

The slight westward tilt but otherwise coherent vortex structure at 1800 UTC 4 September is evident in Fig. 5a. Low-level positive specific humidity anomalies within the AEW trough extend throughout most of the lower troposphere (~600–975 hPa) with a small westward extension of positive anomalies at very low levels (~925 hPa). The low $\theta_e$ air to the west was characterized with specific humidity anomalies below $-4$ g kg$^{-1}$ between 25° and 40°W from the boundary layer up to 700 hPa.

By 1200 UTC 5 September, the closed circulation at 500 hPa had rotated cyclonically to have a northwest (NW)–southeast (SE) alignment with low $\theta_e$ on all sides except the northeast (Fig. 4b). The closed circulation at 850 hPa was centered near the Cape Verde Islands and encompasses a larger area by this time, though was situated below the relative southeasterlies of the 500-hPa circulation (Fig. 4e). On the western edge of the circulation, a very strong moisture gradient is evident throughout the lower troposphere (Fig. 5b). Above 550 hPa the vorticity within the cross section was reduced to below $3 \times 10^{-5}$ s$^{-1}$ and the time series of 850-hPa circulation also shows that at this time the low-level vorticity had started to weaken (Fig. 2). Precipitation was also very weak at this time with only small scattered cells coincident with the overlap of the 500- and 850-hPa circulations.

The result of the continued precession of the horizontal circulations at the top and bottom of the vortex is very apparent by 0600 UTC 6 September, with the midlevel circulation centered around 300 km southwest of the low-level vortex and increasingly collocated with a large region of the low (<332 K) $\theta_e$ air (Fig. 4c). Early morning enhanced convection associated with the AEW trough on 6 September was situated near the center of the low-level circulation around 15°N, 30°W (Fig. 4f). This precipitation, however, was on the northeast periphery of the 500-hPa circulation in a region of wave-relative southerly flow. Although there remained a region of increased (>332 K) $\theta_e$ at 500 hPa that was in vertical alignment with the low-level circulation, the midlevel circulation was now advecting low $\theta_e$ (≤332 K) from the southwest over the low-level vortex. The cross section (Fig. 5c) highlights the lack of organization in the vorticity with two weak but distinct maxima above 700 hPa. The western edge of the AEW midlevel circulation at this time was engulfed with dry air from 500 hPa down to the surface. Though a strong zonal gradient of moisture still exists between the surface up to 600 hPa at around 30°W (Fig. 5c), the continued advection of dry air above and below the wave-relative 500- and 850-hPa circulation centers acts to continue the gradual negative trend of specific humidity in the AEW trough (Fig. 3b). After this time, the vortex gradually weakened and while the weak diurnal peak of convection remains, the amplitude decreases continually each day (Fig. 2).

It is expected that the vertical tilt associated with the AEW trough acted to feed back negatively on the evolution of the convection and associated vorticity generation. As the midlevel vortex is displaced to the west and southwest, the vortex will impose a cyclonic circulation around the tilted column. Because of the weak strength and lack of organization of the vorticity at this time, this feedback is likely slow and relatively small compared to

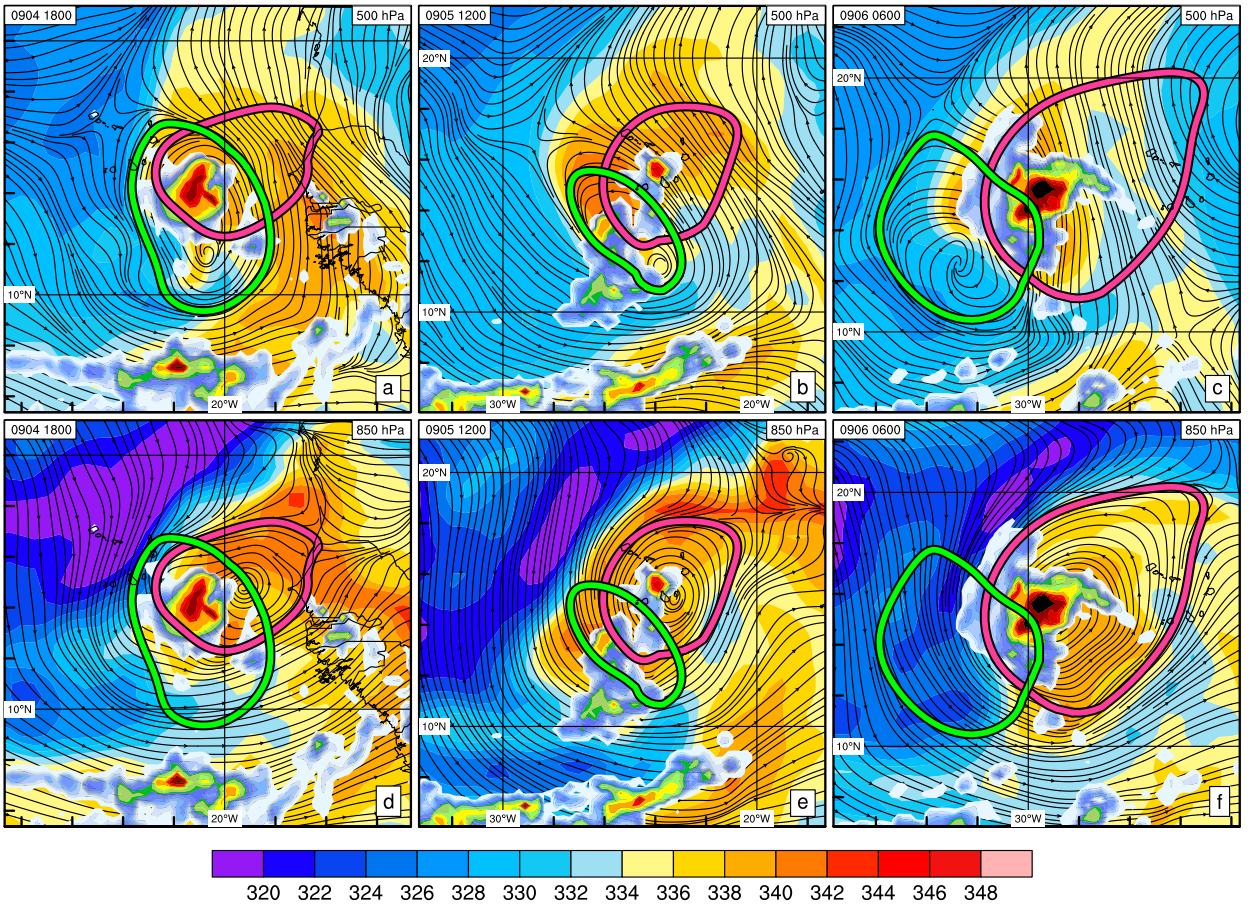


FIG. 4. Equivalent potential temperature (background shading) and wave-relative streamlines for (top) 500 and (bottom) 850 hPa overlaid on both levels is TRMM 3B42 precipitation contoured as in Fig. 1. Maps show data for (a),(d) 1800 UTC 4 Sep; (b),(e) 1200 UTC 5 Sep; and (c),(f) 0600 UTC 6 Sep. For each time, the outermost closed streamline for both isobaric levels are depicted in green (500 hPa) and pink (850 hPa).

tilted TC evolution described by Jones (1995). The vortex associated with the AEW, however, showed a slow cyclonic rotation with the midlevel vortex moving west to southwest of the low-level circulation. Because of the strong horizontal gradients of moisture to the west of the circulation, this vertical tilt also opened the trough up to advecting dry air from the west above or below closed circulations at other levels more rapidly than a coherent vertically aligned vortex would otherwise (e.g., Tang and Emanuel 2010). As the isobaric closed circulations became misaligned vertically environmental air was advected either above and/or below regions of closed circulation. In the case of unfavorable environmental air this is expected to inhibit sustained deep convection and prevent continued intensification of the vortex. Over the eastern Atlantic, where the boundary layer can be as low as 300 m from the surface (Lee et al. 2010), dry air can therefore potentially impact the AEW trough both above and below the maximum vorticity, which is typically collocated with the level of the AEJ.

### b. *Characteristics of the dry air*

The origin and characteristics of dry air over the Atlantic is potentially important with respect to how it impacts TCs and pregenesis tropical disturbances. The previous discussion has shown that a large region of dry air throughout the lower troposphere was present to the west of the AEW trough associated with Invest AL90. Figure 6 shows the evolution of the AEW trough leaving West Africa with 10.7-$\mu$m IR brightness temperature and the split-window IR Saharan air layer product from University of Wisconsin (UW)–Cooperative Institute for Meteorological Satellite Studies (CIMSS) (Dunion and Velden 2004). This product highlights the large area of dry air over the eastern Atlantic to the west and northwest of AL90's convection as the AEW trough and associated convection left the coastal region

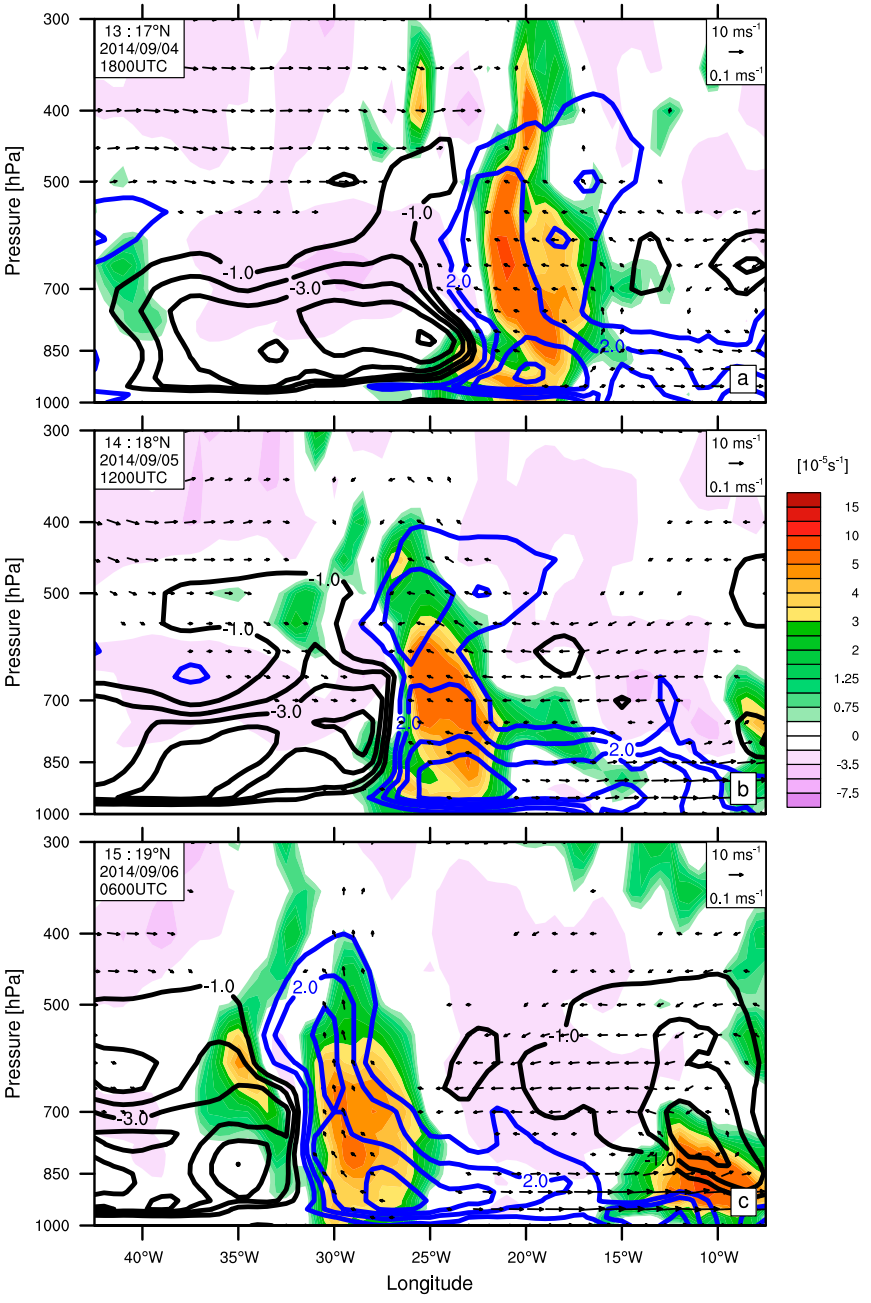


FIG. 5. Vertical cross sections of relative vorticity (shading), anomalous specific humidity (contoured every 1 g kg$^{-1}$), and wave-relative zonal and vertical wind (vectors) for (a) 1800 UTC 4 Sep, (b) 1200 UTC 5 Sep, and (c) 0600 UTC 6 Sep. (Vertical wind vectors have been scaled by 100 for visualization.)

(Fig. 6a). After leaving the coast, as shown previously, the dry and or dusty air wraps around the western edge of the convection from 4 to 5 September with a secondary dry and/or dusty air mass following the trough off the coast on 6 September (Figs. 6b,c). This satellite product, however, does not specifically identify dusty air, rather it highlights dry and/or dusty air at low levels (~925–600 hPa) in cloud-free areas. Subjectively comparing these figures to total dust included in the MERRA2 analysis fields (Fig. 7; and aerosol optical depth measured by MODIS on NASA's *Terra* and *Aqua* satellites; not shown) shows that while dust was present to the west of the disturbance, the highest concentrations are found along the western edge of the circulation. The large area of

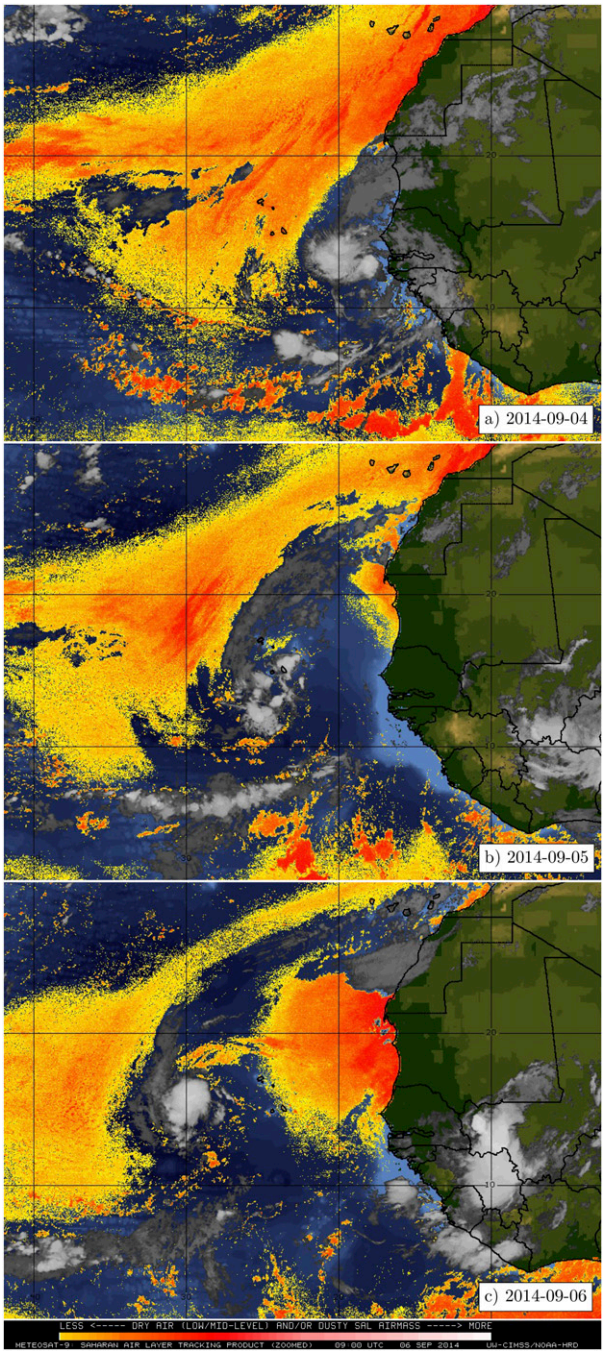


FIG. 6. *Meteosat-9* 10.7-$\mu$m IR imagery overlaid with the IR split-window Saharan air layer tracking product generated by UW–CIMSS. Note the split window algorithm is sensitive to both dry and/or dusty air masses in the lower troposphere (Dunion and Velden 2004).

dry air west and northwest of the system had relatively low concentrations of dust ($<0.5\,\mathrm{mg\,kg^{-1}}$).

Figure 8 shows two vertical cross sections across the western edge of the AEW circulation produced from

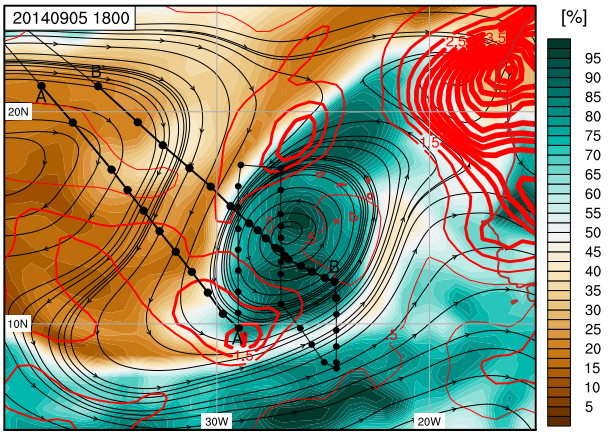


FIG. 7. Relative humidity (shading) and wave-relative streamlines at 800 hPa from MERRA2 for 1800 UTC 5 Sep. Red contours show total dust mixing ratio ($\mathrm{mg\,kg^{-1}}$; 0.5 intervals) integrated through the troposphere. Global Hawk flight track, dropsondes, and cross sections are overlaid. A–A′ and B–B′ indicate limits of the cross section shown in Fig. 8.

Global Hawk dropsonde profiles as well as the aerosol layer detection from the CPL instrument. The Global Hawk made an initial transect from NW to SE between 1800 and 2100 UTC 5 September (Fig. 8a), sampling the environment west of the system and the western side of the AL90 AEW trough (shown on Fig. 7 as A–A′). West of the disturbance between 21°N, 38°W to 14°N, 33°W dry air was observed throughout the troposphere above the boundary layer. While elevated aerosol (yellow) was observed within the boundary layer, the deep layer of dry air above 850 hPa was relatively dust free. The strong inversions seen at the top of the boundary layer (>7 K) and then again at around 550 hPa create an ''onion'' type sounding that is typically of the SAL, but can also be attributed to subsidence (Zipser 1977; Carlson and Prospero 1972, Dunion and Velden 2004). At 14°N, 33°W, a region of increased RH extends farther west from the AEW trough at 600 hPa with dry air observed above and below a shallow layer of moisture. This vertical overlap of moisture highlights the northeast (NE)–southwest (SW)-tilted circulation discussed earlier, with the advection of drier air below the edges of the midlevel circulation. At the end of the transect, SW of the low-level circulation center, increased elevated aerosols are observed, also confirming the small region of high dust concentration along the periphery of the circulation matching well with the dust concentration from MERRA2, which also had the dust concentrated in the layer between 850 and 600 hPa (not shown).

Figure 8b shows the transect as the Global Hawk crossed the circulation from SE to NW (shown on Fig. 7 as B–B′). At this time, the wave-relative streamlines

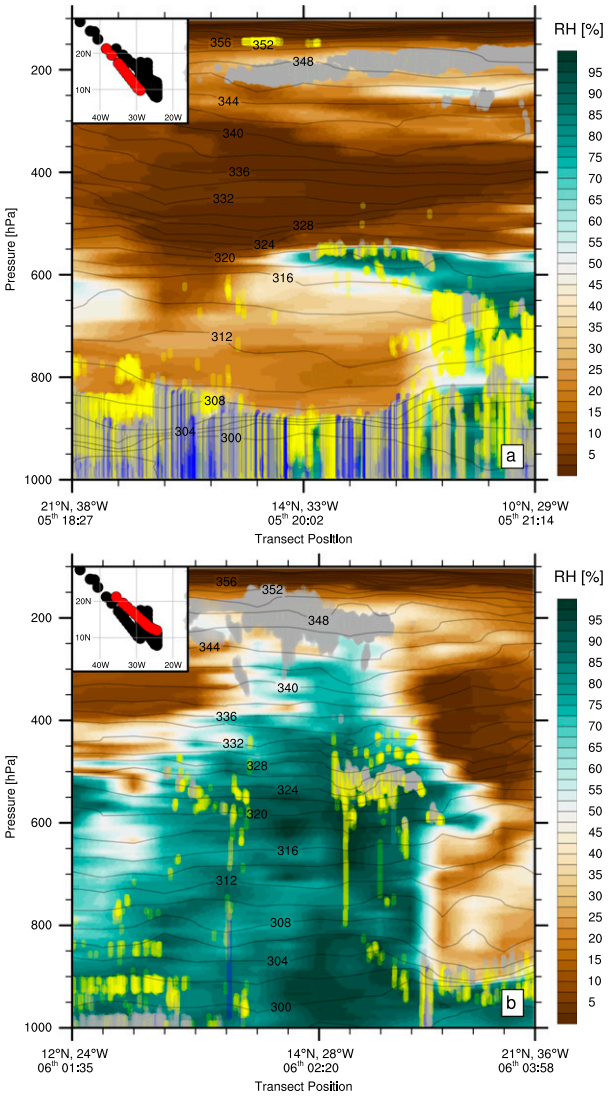


FIG. 8. Cross section of relative humidity (shading), potential temperature (contour lines), and overlaid layer detection as measured by CPL. CPL detects up to eight layers of three types: cloud (gray), elevated aerosol (yellow), and boundary layer (blue). Inset map shows locations of included drops (red) with respect to the all drops (black).

showed that the circulation centers were offset vertically with the midlevel circulation southwest of the low-level circulation (Figs. 5b,e). The cross section in Fig. 8b shows that the trough still had high humidity throughout the column at this time with cloud layers detected up at 200 hPa and thin layers of elevated aerosol detected between 500 and 600 hPa. The gap in aerosol detection around 14°N, 28°W is likely due to thicker clouds and precipitation under the Global Hawk flight level that are obscuring the CPL's detection of cloud and aerosol layers below. As previously discussed, at this time a small burst of deep convection was occurring over the low-level vortex. The northwest quadrant of the circulation shows similar characteristics to the southwest quadrant with a slight extension of the circulation at jet level with dry air above and below. A relatively strong inversion exists at the top of the boundary layer with aerosol and cloud trapped in the boundary layer.

In situ Global Hawk observations highlight and confirm the strength of the horizontal moisture gradient associated with AL90 and its associated AEW circulation, as well as the interaction between the low-level and midlevel dry air in the southwest quadrant of the circulation. The CPL shows that dust was present along the periphery of the moisture associated with the AEW circulation but that the majority of dry air farther from the trough was relatively dust free. It is likely that the dry air west of the disturbance has mixed origins with contribution from the SAL, subtropical subsidence and midlatitude subsidence, and trade-wind flow along the coast.

## 4. Tropical cyclogenesis forecasts

The previous section has highlighted that while the AEW trough designated as Invest AL90 had a convectively active history over Africa, the dry air initially west and then south of the system played a role in inhibiting convection and thus preventing further development over the eastern Atlantic. However, forecast model guidance around the time the AEW trough was leaving the West African coast was suggesting that intensification could occur. The NHC issued its highest probability of genesis within 120 h for AL90 (40%) at 0600 and 1200 UTC 4 September. This indicates that the AEW trough, with weak deep-layer shear, local SSTs >28°C, and active convection prior to reaching the coast, was viewed by the NHC forecasters as having a moderate chance of intensification. Halperin et al. (2013) has shown that the GFS and other models generally have a strong false alarm bias with respect to genesis over the eastern Atlantic, so it is expected that NHC forecasters would have a lower forecast probability when compared to the global models. Tropical Weather Discussions issued by the Tropical Analysis and Forecast Branch (TAFB) of the NHC briefly mention the "dry air engulfing the system" (0805 EDT 4 September 2014) but also focused on the strong convection and "region of deep layer high moisture" around the AEW trough axis. The NHC Tropical Weather Outlooks for AL90 however, do not mention the environmental dry air until the evening of 5 September. This highlights the uncertainty about the fate of this system as well as the need to better understand the key processes that influence the evolution of eastern Atlantic tropical cyclogenesis cases.

This section will consider the evolution of the ensemble forecasts with respect to the evolution of system (AL90) in the CFSv2 analysis. This analysis will explore the variability in the ensemble forecasts of the AEW trough and the sensitivity of intensity forecasts to the surrounding environment. The study will reveal a potential reason for why the GEFS can struggle with over intensification and false alarms of tropical cyclogenesis over the eastern Atlantic.

### *a. Operational forecasts*

Operational forecasts of AL90 for each 0000 UTC 2–5 September cycle from the GEFS are shown in Fig. 9. The ensemble forecast tracks are represented by cones calculated as $\pm 1\sigma$ of across-track spread around the ensemble mean. These forecast tracks highlight that, in general, the GEFS forecasts were able to capture the track of the disturbance quite well. The analysis track consistently falls within the ensemble based cone, although a slight poleward bias is evident for the short-term forecast from 0000 UTC 2 September (Fig. 9a). The GEFS, however, consistently forecasts over intensification of the 850-hPa vortex (Fig. 9b) with corresponding forecasts of too much precipitation in the 24 h after the trough leaves the West African coast (Fig. 9c). The time series of the analysis vorticity and ensemble distribution of forecast vorticity shows that the analysis was weaker than 75% of the forecast ensemble members for all times verifying after 1200 UTC 5 September.

The vertical structure of the ensemble mean vorticity and error with respect to the CFSv2 is presented in Fig. 10 for the four forecasts initialized around the time that AEW trough crossed the West African coast. Each forecast shows an initial slight ($\sim 1 \times 10^{-5}\,s^{-1}$) over intensification of the vorticity around the jet-level over Africa. As the troughs reach the coast the forecast model then consistently overdevelops the low-level vorticity around the trough with ensemble mean errors of over $5 \times 10^{-5}\,s^{-1}$ between the surface and 850 hPa. For the forecast initialized on 4 September (Fig. 10c), although there is overdevelopment of the vortex over the eastern Atlantic between hours 48–72, the forecasts then show a slight weakening trend occurring below 850 hPa in the longer-term forecast evolution (hours 96+). However, the bias remains high as the analysis AEW trough has weakened substantially by this time. Forecasts initialized on 5 September also show a short-term intensification of the low-level vortex, which is then followed by gradual weakening at longer lead times (Fig. 10d). This suggests that despite the intensification of the system in the forecast, the environment still inhibits the longer-term intensity of the disturbance over the Atlantic.

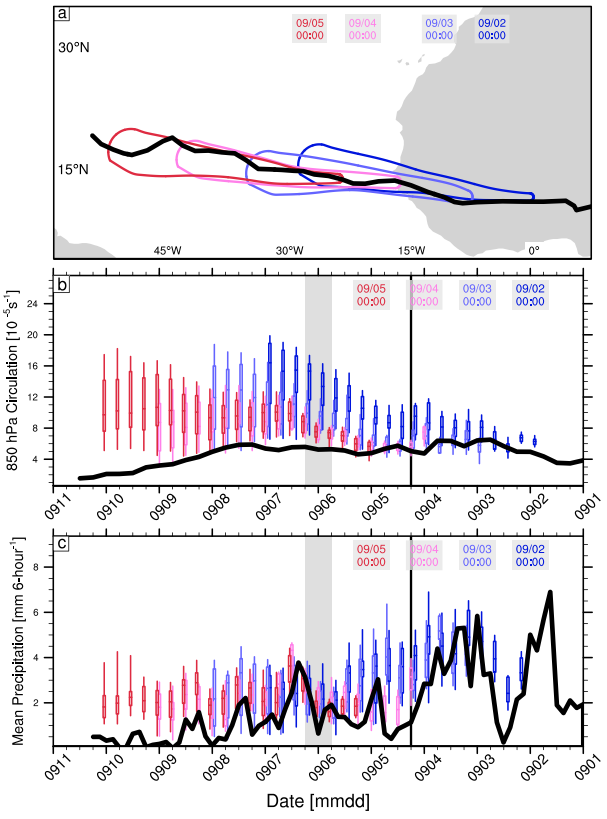


FIG. 9. Ensemble forecasts from the operational GEFS for initializations at 0000 UTC between 2 and 5 Sep. (a) Map displays 120-h forecast cones, created using the ensemble mean track $\pm 1\sigma$ of across-track spread, black line indicates the CFSv2 track. (b) Boxplot distributions of the ensemble forecast 850-hPa circulation (calculated over 300-km radius), analysis (black line) obtained from the CFSv2. (c) Boxplot distributions of the ensemble forecast precipitation (averaged over 500-km radius), analysis (black line) obtained from the TRMM-3B42. For each plot, the colors represent each day's 0000 UTC forecast.

The establishment of a distinctive tilt between the recirculation regions at 500 and 850 hPa by 0600 UTC 6 September was shown in Figs. 4c,f. The associated tilt resulted in advection of dry air below and above the 500- and 850-hPa levels, respectively, which constrained the areal extent of deep convection to the small region of vertical overlap between the circulations. In comparison, Fig. 11 displays snapshots from the four GEFS initialization times for different lead times all verifying 0600 UTC 6 September. The ensemble mean forecast initialized on 2 September (Figs. 11a,b) shows that the 500- and 850-hPa circulations were more vertically aligned than in the analysis (Figs. 4c,f). While there is low (<332 K) $\theta_e$ west of the disturbance, this has not yet wrapped around the southern or southeastern area of the circulation at either the mid- or low levels. Precipitation peaks within the overlapping recirculation

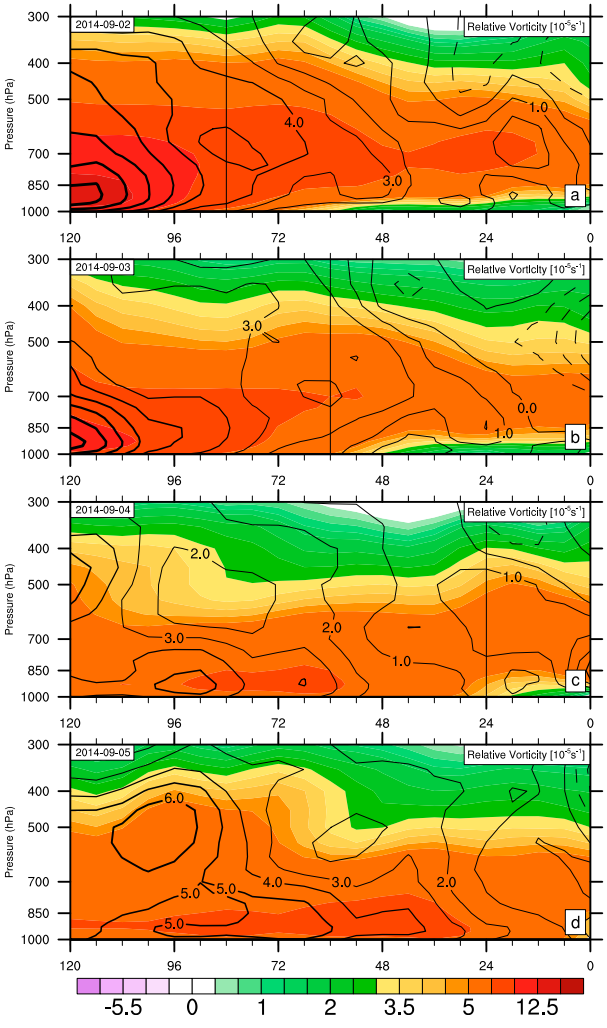


FIG. 10. Ensemble mean forecast evolution of the vertical profile of relative vorticity around each ensembles trough center (shading; $10^{-5}\,s^{-1}$). The ensemble mean error is shown as contours ($10^{-5}\,s^{-1}$). Forecast hour ($x$ axis) increases from right to left, as the trough moves east to west. The vertical black line denotes the trough passage over the coast. Each panel shows a different initialization time displayed in the top-left corner.

areas and there is also a significant amount of precipitation southeast of this in the region of the ITCZ (Fig. 11c). The subsequent forecast initialization depicts a similar ensemble mean structure at forecast hour 78 (Figs. 11d–f). The closed circulations at 500 and 850 hPa are again vertically aligned with precipitation occurring within the overlapping recirculation regions.

GEFS forecasts from the 0000 UTC 4 and 5 September initializations deviate from the two earlier forecasts and are somewhat closer to the analysis state, with less vertical alignment and a weaker midlevel circulation. At forecast hour 54 from the 4 September initialization, the closed circulation at 500 hPa now encompasses $\theta_e$ with values less than 332 K and is situated over low-level $\theta_e$ substantially below 332 K (Figs. 11g,h). The low-level circulation retains high $\theta_e$, but is now below the southerly advection of low $\theta_e$ by the midlevel vortex. Precipitation rates, however, show little change from those in the earlier forecasts with a peak occurring in the small region of vertical alignment between the 500- and 850-hPa circulations (Fig. 11i).

As the forecast lead time gets shorter the forecast of the midlevel circulation continues to weaken toward the verifying analysis state. Lower $\theta_e$ now has almost completely encircled both the mid- and low-level circulations. (Figs. 11j,k). The circulation at 500 hPa has only a very small area of closed circulation with the main vortex farther west in low $\theta_e$ air. Precipitation is still forecast to maintain intensity and areal extent despite the decreasing favorability of the midlevel environment. Precipitation south of the circulation has however now disconnected from the zonal strip south of 10°N.

The mean GEFS ensemble forecasts show consistent errors or biases across multiple initializations. Forecast track location is reasonably accurate, but the vortex associated with the AEW trough has a consistent positive intensity bias over Africa that increases over the eastern Atlantic. The over intensification of the vortex produces a circulation that is too strong through the lower troposphere and, therefore, does not accurately interact with the unfavorable environmental air west of the disturbance. Comparison of the forecast ensemble structure for times verifying at 0600 UTC 6 September show that the longer-range forecasts have more vertically aligned and convectively active disturbances that are mostly protected from the dry environmental air to the west. Later initializations with shorter lead times portray a weaker and shallower circulation that has started to advect the low $\theta_e$ across multiple levels of the circulation. Precipitation, however, retains intensity over the core of the low-level circulation. Given the horizontal resolution of the GEFS forecasts and the parameterized convective scheme used, it is expected that this persistence of convection and apparent lack of sensitivity to the environment is likely a primary cause in the general over intensification at low levels across all GEFS ensembles and initializations.

### *b. Ensemble-based sensitivity analysis*

The previous section has discussed the evolution of the GEFS ensemble members on average and while the forecasts consistently over intensified the low-level vortex, there was also large spread across the distribution. These forecasts can therefore potentially provide more information about the intensification of pregenesis disturbances over the eastern Atlantic. To understand

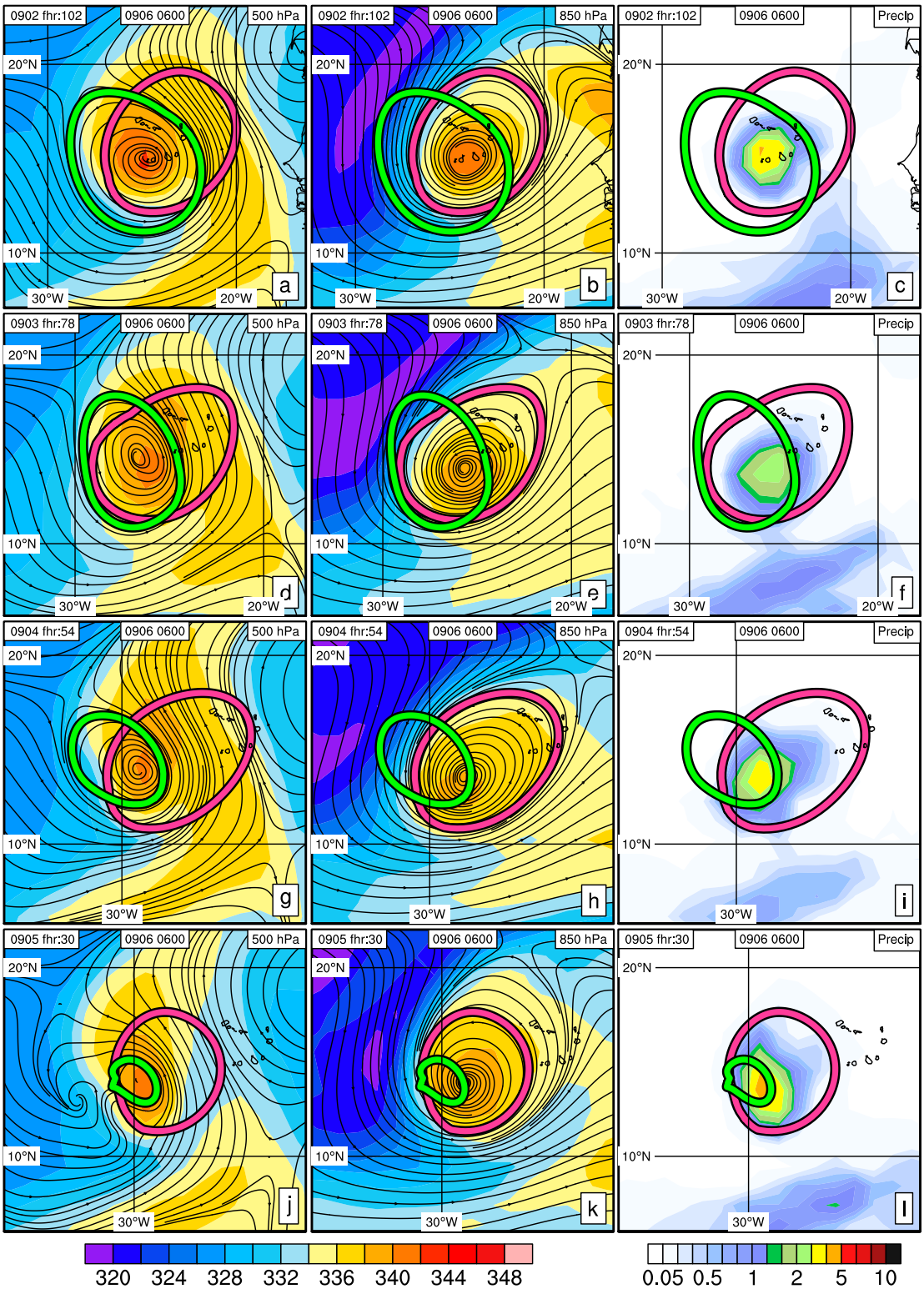


FIG. 11. Ensemble mean forecast fields from four different initialization times (rows) all verifying for 0000 UTC 6 Sep. Columns show forecast equivalent potential temperature (K) and wave-relative streamlines for (a),(d),(g),(j) 500 hPa and (b),(e),(h),(k) 850 hPa and (c),(f),(i),(l) forecast precipitation (mm $h^{-1}$). All three columns include the outermost closed streamlines at 500 (green) and 850 hPa (pink).

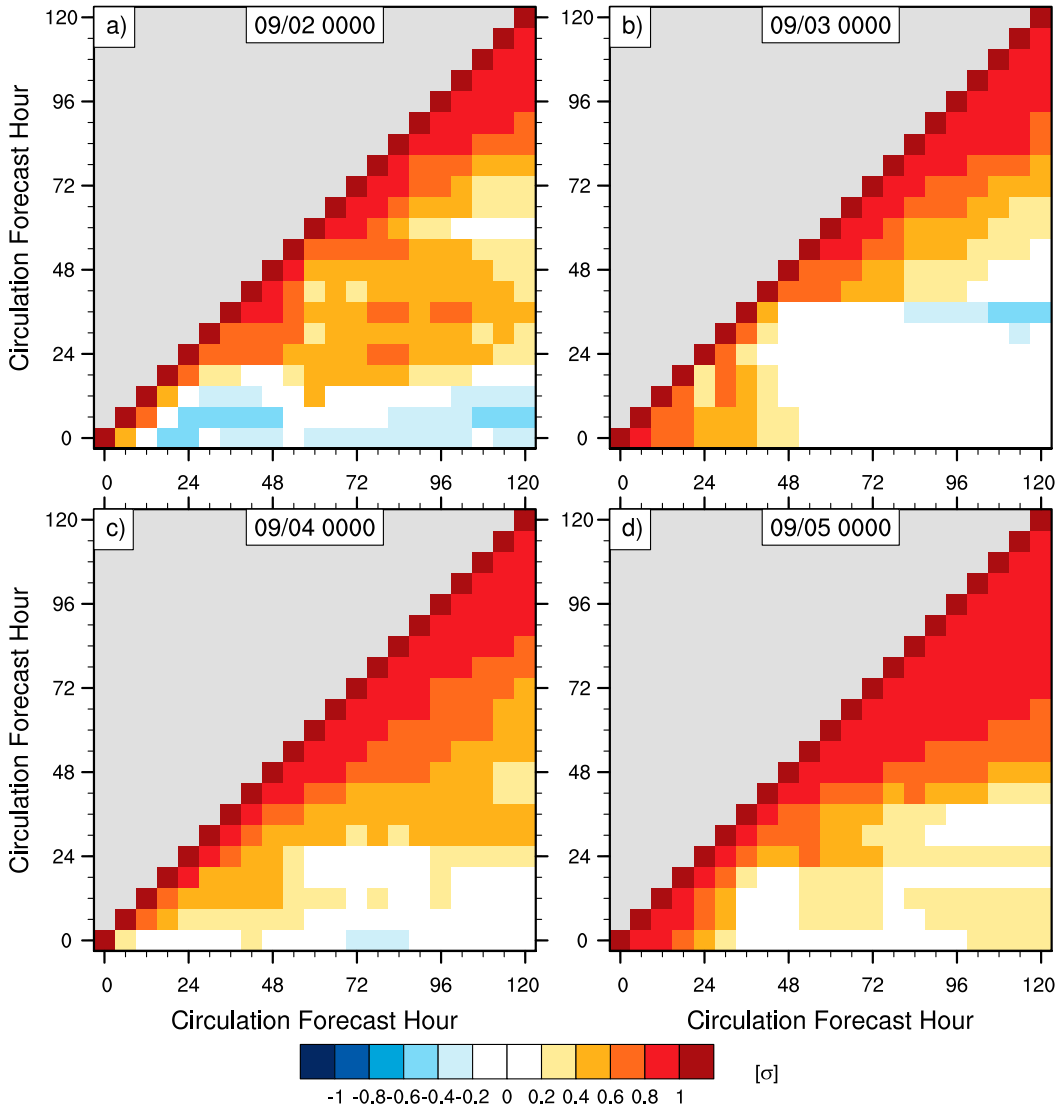


FIG. 12. Autocorrelation between the intensity of the 850-hPa circulation calculated over a 300-km radius around the ensemble forecast troughs with intensity of the circulation at subsequent lead times. Colored boxes show the strength of correlation across the ensemble distribution at lagged forecast times. Panels show different initialization times.

the variability in the GEFS intensity evolution across the ensemble members, the ensemble member vortex strengths at each forecast hour were correlated with the strength of the vortex at each subsequent forecast hour (Fig. 12). Positive correlation indicates that strong ensemble members stay strong and weaker members stay weaker. Therefore, this effectively shows how long the forecast retains a linear signal about the ensemble distribution at an earlier forecast time. For the 0000 UTC 2 September ensemble forecast, there is a negative correlation between the vortex strength at hours 0–18 and vortex strength at later lead times (Fig. 12a). This shows that ensemble members initialized with a stronger vortex tend to end up on the weak side of the ensemble distribution after 24 h. At forecast hour 24, there is significant positive autocorrelation for the strength of the vortex at all subsequent hours.

A similar signal of autocorrelation for vortex strength is seen across the subsequent initialization times. Forecasts initialized at 0000 UTC 3 September show low correlation values with respect to vortex strength over the first 36 h, but at hour 42 a significant correlation becomes evident for the subsequent 72 h (Fig. 12b). Once the vortex is over the ocean during 4–5 September, the autocorrelation becomes more consistent with the 24–30-h vortex strength and exhibits significant correlation with

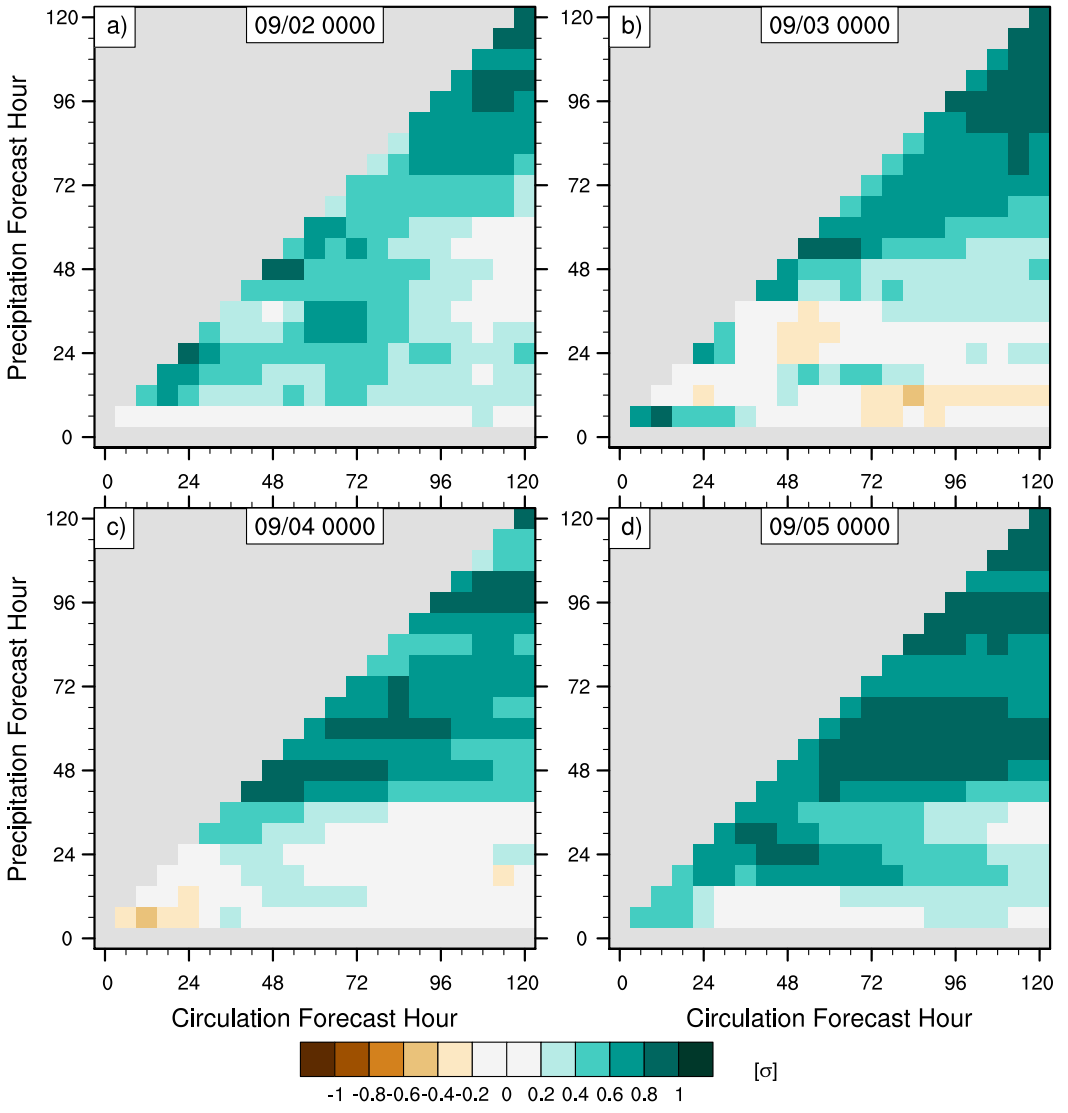


FIG. 13. Intraensemble correlation between the precipitation within 300 km of ensemble forecast vortex with the intensity of the 850-hPa circulation calculated over a 300-km radius at subsequent lead times. Colored boxes show strength of correlation across the ensemble distribution at lagged forecast times. Panels show different initialization times.

the strength of the vortex through the remaining forecast hours (Figs. 12c,d). These figures indicate the time at which strong GEFS ensemble members will stay strong and weak members stay weaker, or that beyond this point the evolution of the system is relatively linear and a function of the vortex strength. For these 4 GEFS ensemble forecasts, understanding the 120-h vortex strength is typically dependent on understanding the evolution of the vortex over the first 24–48 h.

Figure 13 shows the correlation of mean precipitation within 300 km of the trough center and the future strength of the 850-hPa vortex. Precipitation in the first 24–48 h of the forecasts consistently has significant correlation with the vortex strength throughout the remaining forecasts, comparable to the vortex strength autocorrelation shown in Fig. 12. Vortex stretching through diabatic heating is likely the primary method for vorticity generation throughout this time; therefore, understanding the influences on the short-term precipitation forecasts is crucial to understanding the later evolution of the vortex. These figures highlight that after a certain lead time, hours 24–48 for these forecasts, the evolution of the vortex becomes largely dependent on its the strength and convective activity at earlier lead times. Members that continue to intensify have likely developed a closed circulation and are less sensitive to

the surrounding environment, while weaker members may have weakened to the point where they cannot reintensify given the hostile environment to the west of the circulation.

Ensemble sensitivity analysis will be utilized to understand the variability in precipitation forecasts over the first 24–48 h of each forecast cycle. This method correlates state variables across the ensemble with an ensemble forecast metric at some later lead time. Precipitation around the vortex was generally significantly correlated with the 120-h vortex strength as early as forecast hour 42. This metric will be regressed against the trough-relative lower-tropospheric (900–700 hPa) moist static energy at forecast hour 12 (Fig. 14). For the forecast initialized on 2 September, the main areas of sensitivity are north of the vortex, where an increase of moist static energy is related to increased precipitation in the trough 30 h later or south of the disturbance where an inverse relationship is observed (Fig. 14a). The wave-relative streamlines for this time, show a fairly small but also closed circulation in the lower troposphere, with strong meridional flow on the western edge of the AEW trough. Trajectory analysis for AEWs in this region has shown a similar structure with very few eastern Atlantic trajectories entrained in to the vortex while the trough was still over the continent (Brammer and Thorncroft 2017).

When the AEW trough reaches the coastal region of West Africa and moves over the eastern Atlantic, the area of sensitivity shifted to the northwest and west of the vortex (Figs. 14b–d). The sensitivity follows the region and gradient of the dry air on the western edge of the AEW trough as it is wrapped around the vortex. South of the vortex there is a consistent region of sensitivity with a negative correlation, showing that lower moist static energy in this region is associated with increased precipitation in the trough. A similar signal was also observed in composites of developing and nondeveloping AEWs in Brammer and Thorncroft (2015). This sensitivity is on a thin zonal strip of increased moist static energy associated with the ITCZ, which can be seen in the analysis of $\theta_e$ in Fig. 5, and related to a meridional shift of the ITCZ moisture toward the vortex creating drier conditions on the equatorward gradient.

Analysis of the differences in the GEFS ensemble member evolutions has highlighted that short-term errors in precipitation and vorticity generation can have significant impact on the long-term forecasts. A feedback loop is proposed whereby active convection enhances vorticity, creating a vertically aligned and coherent circulation in the lower troposphere, which provides a favorable area for continued convection. For cases that have favorable trough-scale conditions, short-term positive bias in precipitation is expected to trigger

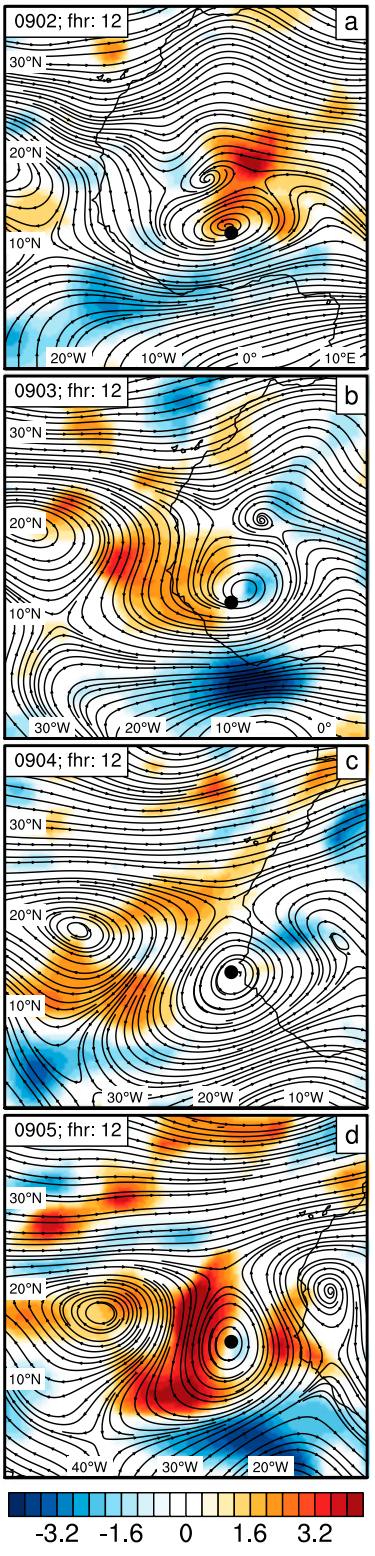


FIG. 14. Trough-relative streamlines layer averaged between 900 and 700 hPa. Shading shows sign and significance of the ensemble-based 42-h precipitation forecast sensitivity to layer average moist static energy ($\sigma$). Positive shading denotes increased moist static energy at that location is significantly correlated to increased precipitation in the trough at hour 42.

this feedback loop resulting in the analysis verifying outside of the whole distribution of the ensemble members. Short-term sensitivity analysis for precipitation occurring in the AEW trough shows that convective activity is sensitive to environmental moisture to the north of the circulation over West Africa and northwest to west once over the eastern Atlantic. These regions align with the mean low-level inflow of air into AEW troughs as shown with trajectory analysis by Brammer and Thorncroft (2017).

## 5. Discussion

The analysis presented in this paper has documented the evolution of an intense African easterly wave (AEW; Invest AL90) during the peak of the 2014 Atlantic hurricane season. As the AEW crossed the West African coast, NHC forecasted a moderate 120-h probability of cyclogenesis occurring over the eastern Atlantic (40%; 0200 EDT 4 September). Typical conditions for genesis appeared favorable with weak deep-layer vertical shear, SSTs around 28°C, and a moist and convectively active precursor disturbance. In the following days, however, the AEW trough lacked widespread organized convection as it interacted with a large region of dry air to the west and north of the circulation that ultimately hindered it from developing into a tropical cyclone.

During the AEWs' life over the African continent, there were repeated diurnal bursts of convection associated with the strong jet-level vortex that likely contributed to the strength of the system (Berry and Thorncroft 2012). After leaving the continent and emerging over the eastern Atlantic, however, precipitation was substantially restricted in spatial extent within the AEW trough. During this time, dry air from the northwest had created a strong moisture gradient along the western edge of the circulation and was being wrapped around the circulation to the south. Wave-relative streamline analysis showed that after the AEW trough left the West African coast, there was an increasing misalignment between the AEW's midlevel and low-level circulations. It is hypothesized that the circulation initially becomes misaligned because of the shallow vertical shear imposed by the AEJ over the eastern Atlantic. Subsequently, the displaced circulations at mid- and lower levels induce flows that interact with the other's circulation resulting in the low- to midlevel circulations slowly rotating cyclonically with respect to each other (Jones 1995). Misalignment of the centroids of the low- and midlevel circulations then enabled the horizontal advection of unfavorable low $\theta_e$ air into the AEW trough, restricting the area of deep convection and inhibiting further vorticity generation. The importance of vertically aligned circulations for TC genesis has been shown in other cases across the basin in regions of unfavorable environments (e.g., Raymond and Carrillo 2011; Wang 2012; Davis and Ahijevych 2012; Fritz and Wang 2014). The shallow layer shear imposed by the midlevel AEJ is likely a common factor for AEWs leaving West Africa; in marginal cases such as this where dry air is present and convection is therefore reduced, the vortex is thus weakened and unable to retain a coherent circulation.

In situ observations from the NASA Global Hawk confirm the representation of the dry air in both the CFSv2 and MERRAv2 analysis and the interaction between the circulation at 700–600 hPa with dry air above and below as the tropical disturbance moved over the eastern Atlantic. The onboard NASA Cloud Physics Lidar also highlighted that the dry air over the eastern Atlantic was relatively dust free except for a narrow strip along the western edge of the AEW circulation, highlighting the multiorigin nature of dry air outbreaks over the eastern Atlantic (Braun 2010; Brammer and Thorncroft 2017). Increased aerosol concentrations were observed and also represented in the MERRA-2 reanalysis along the moisture gradient of the AEW circulation, highlighting an important contribution of SAL to the dry air. The interactions discussed here, however, do not consider the impact of dust on the evolution of AL90 and its associated AEW trough. The GEFS model does not include the radiative impact of dust and therefore our analysis is limited in addressing its relative contribution.

Ensemble forecasts from the operational GFS model were used to assess the differences across the ensemble distributions of the forecasts as well as the systematic bias observed with the GFS. Biases in the deterministic forecasts have been shown over the eastern Atlantic through high rates of false alarms for tropical cyclogenesis (Halperin et al. 2013). The GEFS ensemble forecast track of the AEW trough was relatively skillful with the analysis typically falling within $\pm 1$ standard deviation of the mean; however, there was a consistent over intensification of the low-level vortex as it transitioned over the coastal region. The over intensification of the vortex was associated with short-term precipitation errors that led to increased vorticity and a vertically aligned circulation over the eastern Atlantic. Storm-relative ensemble mean plots of the wave-relative streamlines reveal that the forecasts consistently had a vertically aligned circulation with a relatively broad area of convection.

Autocorrelation of the ensemble characteristics showed that the 120-h forecast vortex intensity was largely

dependent on the characteristics of the vortex after the first 24–48 h of the forecast. Torn and Cook (2013) showed a similar relation with small errors in the short-term boundary layer and lower-tropospheric moisture content significantly impacting the long-term evolution. For AEW troughs entering a marginal environment characterized by weak deep-layer vertical shear, warms SSTs, but dry air throughout the lower troposphere, it is suggested that small errors can feed back onto the long-term evolution of intensity forecasts for these incipient tropical disturbances. Short-term precipitation forecast errors can result in the whole ensemble distribution over intensifying the AEW circulation, which can limit the forecasted interaction with the hostile environment to the west, thereby enabling continued convection and the associated vorticity generation.

Given the false alarm bias shown in the deterministic GFS forecasts over the eastern Atlantic and a similar bias with respect to diabatic heating and low-level vorticity in the CFSR reanalysis (Janiga and Thorncroft 2013), further analysis of more nondeveloping tropical disturbances in this region is recommended to understand the processes that limit convection in strong vortices and lead to the demise of the once favorable characteristics associated with such disturbances. Understanding the synoptic-scale interaction between AEW circulations and the environment is also important in identifying situations where a small error in the short-term model forecast may be propagated downstream. The West African coastal region where this sensitivity appears to be crucial has a relatively sparse observation network. This study highlights the need for more observations in this region to improve our knowledge of the key processes as well as improving the initial conditions in NWP models.

*Acknowledgments.* This research is supported in part by NASA Grant NNX10AU44G on the Hurricane Severe Storm Sentinel (HS3) campaign and NOAA NA15NWS4680005. The authors would like to thank the two reviewers for their helpful and thorough comments. The authors wish to acknowledge the NASA HS3 program for providing both scientific motivation and Global Hawk aircraft data for this study. The CFSR and CFSv2 data used in this study were downloaded from the Research Data Archive (RDA), which is maintained by the Computational and Information Systems Laboratory (CISL) at the National Center for Atmospheric Research (NCAR). NCAR is sponsored by the National Science Foundation (NSF). Analysis and plotting of data were conducted using the NCAR Command Language (version 6.3.0) [Software] (2014). Boulder, Colorado: UCAR/NCAR/CISL/VETS. http://dx.doi.org/10.5065/D6WD3XH5.

## REFERENCES

Arnault, J., and F. Roux, 2009: Case study of a developing African easterly wave during NAMMA: An energetic point of view. *J. Atmos. Sci.*, **66**, 2991–3020, https://doi.org/10.1175/2009JAS3009.1.

——, and ——, 2010: Comparison between two case studies of developing and nondeveloping African easterly waves during NAMMA and AMMA/SOP-3: Absolute vertical vorticity budget. *Mon. Wea. Rev.*, **138**, 1420–1445, https://doi.org/10.1175/2009MWR3120.1.

Berry, G. J., and C. D. Thorncroft, 2005: Case study of an intense African easterly wave. *Mon. Wea. Rev.*, **133**, 752–766, https://doi.org/10.1175/MWR2884.1.

——, and ——, 2012: African easterly wave dynamics in a mesoscale numerical model: The upscale role of convection. *J. Atmos. Sci.*, **69**, 1267–1283, https://doi.org/10.1175/JAS-D-11-099.1.

Bracken, W. E., and L. F. Bosart, 2000: The role of synoptic-scale flow during tropical cyclogenesis over the North Atlantic Ocean. *Mon. Wea. Rev.*, **128**, 353–376, https://doi.org/10.1175/1520-0493(2000)128<0353:TROSSF>2.0.CO;2.

Brammer, A., and C. D. Thorncroft, 2015: Variability and evolution of African easterly wave structures and their relationship with tropical cyclogenesis over the eastern Atlantic. *Mon. Wea. Rev.*, **143**, 4975–4995, https://doi.org/10.1175/MWR-D-15-0106.1.

——, and ——, 2017: Spatial and temporal variability of the three-dimensional flow around African easterly waves. *Mon. Wea. Rev.*, **145**, 2879–2895, https://doi.org/10.1175/MWR-D-16-0454.1.

Braun, S. A., 2010: Reevaluating the role of the Saharan air layer in Atlantic tropical cyclogenesis and evolution. *Mon. Wea. Rev.*, **138**, 2007–2037, https://doi.org/10.1175/2009MWR3135.1.

——, P. A. Newman, and G. M. Heymsfield, 2016: NASA's Hurricane and Severe Storm Sentinel (HS3) investigation. *Bull. Amer. Meteor. Soc.*, **97**, 2085–2102, https://doi.org/10.1175/BAMS-D-15-00186.1.

Burpee, R., 1972: The origin and structure of easterly waves in the lower troposphere of North Africa. *J. Atmos. Sci.*, **29**, 77–90, https://doi.org/10.1175/1520-0469(1972)029<0077:TOASOE>2.0.CO;2.

——, 1974: Characteristics of North African easterly waves during the summers of 1968 and 1969. *J. Atmos. Sci.*, **31**, 1556–1570, https://doi.org/10.1175/1520-0469(1974)031<1556:CONAEW>2.0.CO;2.

Carlson, T. N., 1969a: Some remarks on African disturbances and their progress over the tropical Atlantic. *Mon. Wea. Rev.*, **97**, 716–726, https://doi.org/10.1175/1520-0493(1969)097<0716:SROADA>2.3.CO;2.

——, 1969b: Synoptic histories of three African disturbances that developed into Atlantic hurricanes. *Mon. Wea. Rev.*, **97**, 256–276, https://doi.org/10.1175/1520-0493(1969)097<0256:SHOTAD>2.3.CO;2.

——, and J. M. Prospero, 1972: The large-scale movement of Saharan air outbreaks over the northern equatorial Atlantic. *J. Appl. Meteor.*, **11**, 283–297, https://doi.org/10.1175/1520-0450(1972)011<0283:TLSMOS>2.0.CO;2.

Chiao, S., and G. S. Jenkins, 2010: Numerical investigations on the formation of Tropical Storm Debby during NAMMA-06. *Wea. Forecasting*, **25**, 866–884, https://doi.org/10.1175/2010WAF2222313.1.

Davis, C. A., and D. A. Ahijevych, 2012: Mesoscale structural evolution of three tropical weather systems observed during PREDICT. *J. Atmos. Sci.*, **69**, 1284–1305, https://doi.org/10.1175/JAS-D-11-0225.1.

Dieng, A. L., S. M. Sall, A. Lazar, M. Leduc-Leballeur, and L. Eymard, 2014: Analysis of strengthening and dissipating mesoscale convective systems propagating off the West

African coast. *Mon. Wea. Rev.*, **142**, 4600–4623, https://doi.org/10.1175/MWR-D-13-00388.1.

Dunion, J. P., 2011: Rewriting the climatology of the tropical North Atlantic and Caribbean Sea atmosphere. *J. Climate*, **24**, 893–908, https://doi.org/10.1175/2010JCLI3496.1.

——, and C. S. Velden, 2004: The impact of the Saharan air layer on Atlantic tropical cyclone activity. *Bull. Amer. Meteor. Soc.*, **85**, 353–365, https://doi.org/10.1175/BAMS-85-3-353.

Dunkerton, T., M. Montgomery, and Z. Wang, 2009: Tropical cyclogenesis in a tropical wave critical layer: Easterly waves. *Atmos. Chem. Phys.*, **9**, 5587–5646, https://doi.org/10.5194/acp-9-5587-2009.

Frank, N. L., 1970: Atlantic tropical systems of 1969. *Mon. Wea. Rev.*, **98**, 307–314, https://doi.org/10.1175/1520-0493(1970)098<0307:ATSO>2.3.CO;2.

Freismuth, T. M., B. Rutherford, M. A. Boothe, and M. T. Montgomery, 2016: Why did the storm ex-Gaston (2010) fail to redevelop during the PREDICT experiment? *Atmos. Chem. Phys.*, **16**, 8511–8519, https://doi.org/10.5194/acp-16-8511-2016.

Fritz, C., and Z. Wang, 2013: A numerical study of the impacts of dry air on tropical cyclone formation: A development case and a nondevelopment case. *J. Atmos. Sci.*, **70**, 91–111, https://doi.org/10.1175/JAS-D-12-018.1.

——, and ——, 2014: Water vapor budget in a developing tropical cyclone and its implication for tropical cyclone formation. *J. Atmos. Sci.*, **71**, 4321–4332, https://doi.org/10.1175/JAS-D-13-0378.1.

Gray, W., 1968: Global view of the origin of tropical disturbances and storms. *Mon. Wea. Rev.*, **96**, 669–700, https://doi.org/10.1175/1520-0493(1968)096<0669:GVOTOO>2.0.CO;2.

Halperin, D. J., H. E. Fuelberg, R. E. Hart, J. H. Cossuth, P. Sura, and R. J. Pasch, 2013: An evaluation of tropical cyclone genesis forecasts from global numerical models. *Wea. Forecasting*, **28**, 1423–1445, https://doi.org/10.1175/WAF-D-13-00008.1.

Hock, T. F., and J. L. Franklin, 1999: The NCAR GPS dropwindsonde. *Bull. Amer. Meteor. Soc.*, **80**, 407–420, https://doi.org/10.1175/1520-0477(1999)080<0407:TNGD>2.0.CO;2.

Hopsch, S. B., C. D. Thorncroft, and K. R. Tyle, 2010: Analysis of African easterly wave structures and their role in influencing tropical cyclogenesis. *Mon. Wea. Rev.*, **138**, 1399–1419, https://doi.org/10.1175/2009MWR2760.1.

Huffman, G. J., and Coauthors, 2007: The TRMM Multisatellite Precipitation Analysis (TMPA): Quasi-global, multiyear, combined-sensor precipitation estimates at fine scales. *J. Hydrometeor.*, **8**, 38–55, https://doi.org/10.1175/JHM560.1.

Janiga, M. A., and C. D. Thorncroft, 2013: Regional differences in the kinematic and thermodynamic structure of African easterly waves. *Quart. J. Roy. Meteor. Soc.*, **139**, 1598–1614, https://doi.org/10.1002/qj.2047.

Jones, S. C., 1995: The evolution of vortices in vertical shear. I: Initially barotropic vortices. *Quart. J. Roy. Meteor. Soc.*, **121**, 821–851, https://doi.org/10.1002/qj.49712152406.

Komaromi, W. A., and S. J. Majumdar, 2015: Ensemble-based error and predictability metrics associated with tropical cyclogenesis. Part II: Wave-relative framework. *Mon. Wea. Rev.*, **143**, 1665–1686, https://doi.org/10.1175/MWR-D-14-00286.1.

Landsea, C. W., 1993: A climatology of intense (or major) Atlantic hurricanes. *Mon. Wea. Rev.*, **121**, 1703–1713, https://doi.org/10.1175/1520-0493(1993)121<1703:ACOIMA>2.0.CO;2.

Lee, J. D., and Coauthors, 2010: Reactive Halogens in the Marine Boundary Layer (RHaMBLe): The tropical North Atlantic experiments. *Atmos. Chem. Phys.*, **10**, 1031–1055, https://doi.org/10.5194/acp-10-1031-2010.

Leppert, K. D., II, D. J. Cecil, and W. A. Petersen, 2013a: Relation between tropical easterly waves, convection, and tropical cyclogenesis: A Lagrangian perspective. *Mon. Wea. Rev.*, **141**, 2649–2668, https://doi.org/10.1175/MWR-D-12-00217.1.

——, W. A. Petersen, and D. J. Cecil, 2013b: Electrically active convection in tropical easterly waves and implications for tropical cyclogenesis in the Atlantic and east Pacific. *Mon. Wea. Rev.*, **141**, 542–556, https://doi.org/10.1175/MWR-D-12-00174.1.

Marchok, T. P., 2002: How the NCEP tropical cyclone tracker works. Preprints, *25th Conf. on Hurricanes and Tropical Meteorology*, San Diego, CA, Amer. Meteor. Soc., 21–22.

Raymond, D. J., and C. L. Carrillo, 2011: The vorticity budget of developing typhoon Nuri (2008). *Atmos. Chem. Phys.*, **11**, 147–163, https://doi.org/10.5194/acp-11-147-2011.

Rios-Berrios, R., R. D. Torn, and C. A. Davis, 2016: An ensemble approach to investigate tropical cyclone intensification in sheared environments. Part I: Katia (2011). *J. Atmos. Sci.*, **73**, 71–93, https://doi.org/10.1175/JAS-D-15-0052.1.

Saha, S., and Coauthors, 2010: The NCEP Climate Forecast System Reanalysis. *Bull. Amer. Meteor. Soc.*, **91**, 1015–1057, https://doi.org/10.1175/2010BAMS3001.1.

——, and Coauthors, 2014: The NCEP Climate Forecast System Version 2. *J. Climate*, **27**, 2185–2208, https://doi.org/10.1175/JCLI-D-12-00823.1.

Tang, B., and K. A. Emanuel, 2010: Midlevel ventilation's constraint on tropical cyclone intensity. *J. Atmos. Sci.*, **67**, 1817–1830, https://doi.org/10.1175/2010JAS3318.1.

Torn, R. D., 2010: Ensemble-based sensitivity analysis applied to African easterly waves. *Wea. Forecasting*, **25**, 61–78, https://doi.org/10.1175/2009WAF2222255.1.

——, and D. Cook, 2013: The role of vortex and environment errors in genesis forecasts of Hurricanes Danielle and Karl (2010). *Mon. Wea. Rev.*, **141**, 232–251, https://doi.org/10.1175/MWR-D-12-00086.1.

Ventrice, M. J., C. D. Thorncroft, and M. A. Janiga, 2012: Atlantic tropical cyclogenesis: A three-way interaction between an African easterly wave, diurnally varying convection, and a convectively coupled atmospheric Kelvin wave. *Mon. Wea. Rev.*, **140**, 1108–1124, https://doi.org/10.1175/MWR-D-11-00122.1.

Vomel, H., T. F. Hock, and K. Young, 2016: NCAR/EOL Technical Note Dropsonde Dry Bias. NCAR Tech. Note, NCAR, 7 pp.

Wang, J., and Coauthors, 2010: Water vapor variability and comparisons in the subtropical Pacific from The Observing System Research and Predictability Experiment-Pacific Asian Regional Campaign (T-PARC) Driftsonde, Constellation Observing System for Meteorology, Ionosphere, and Climate (COSMIC), and reanalyses. *J. Geophys. Res.*, **115**, D21108, https://doi.org/10.1029/2010JD014494.

Wang, Z., 2012: Thermodynamic aspects of tropical cyclone formation. *J. Atmos. Sci.*, **69**, 2433–2451, https://doi.org/10.1175/JAS-D-11-0298.1.

——, and I. Hankes, 2014: Characteristics of tropical easterly wave pouches during tropical cyclone formation. *Mon. Wea. Rev.*, **142**, 626–633, https://doi.org/10.1175/MWR-D-13-00267.1.

Zipser, E. J., 1977: Mesoscale and convective-scale downdrafts as distinct components of squall-line structure. *Mon. Wea. Rev.*, **105**, 1568–1589, https://doi.org/10.1175/1520-0493(1977)105<1568:MACDAD>2.0.CO;2.